



**HAL**  
open science

# Measurement of extensional properties during free jet breakup

Christophe Tirel, Marie-Charlotte Renoult, Christophe Dumouchel

► **To cite this version:**

Christophe Tirel, Marie-Charlotte Renoult, Christophe Dumouchel. Measurement of extensional properties during free jet breakup. *Experiments in Fluids*, 2020, 61 (2), 10.1007/s00348-019-2845-8 . hal-02442431

**HAL Id: hal-02442431**

**<https://normandie-univ.hal.science/hal-02442431>**

Submitted on 3 Jun 2020

**HAL** is a multi-disciplinary open access archive for the deposit and dissemination of scientific research documents, whether they are published or not. The documents may come from teaching and research institutions in France or abroad, or from public or private research centers.

L'archive ouverte pluridisciplinaire **HAL**, est destinée au dépôt et à la diffusion de documents scientifiques de niveau recherche, publiés ou non, émanant des établissements d'enseignement et de recherche français ou étrangers, des laboratoires publics ou privés.

# Measurement of extensional properties during free jet breakup

Christophe Tirel · Marie-Charlotte Renoult · Christophe Dumouchel

Received: date / Accepted: date

**Abstract** This paper reports an experimental method for extracting the extensional properties of viscoelastic liquids during atomization. As a first approach, low-velocity free jets are considered. Such jets of viscoelastic liquids break with the formation of a beads-on-a-string pattern composed of quasi-spherical beads and quasi-cylindrical ligaments. The liquid extensional properties, i.e., the relaxation time and the terminal extensional viscosity, are measured by analyzing the ligament thinning. This analysis uses a statistical multi-scale description tool whose principle is explained for an ensemble of thinning cylinders. The tool is applied to free jets of dilute polymer solutions for several polymer concentrations, liquid flow rates and nozzle dimensions. Results show a correlation between the terminal extensional viscosity and the relaxation time in good agreement with the literature. The relaxation time is found to depend on an equivalent nozzle deformation rate. This behavior is due to polymer mechanical degradation in the nozzle. Because of its statistical nature, the method also returns the diameter distribution of the ligaments seen at each position along the jet. Ligament diameter distributions observed in more energetic atomization processes can thus be measured. The extensional properties can also be inferred from a temporal monitoring of these ligaments.

**Keywords** Viscoelasticity · dilute polymer solution · atomization · free liquid jet · multi-scale analysis

Marie-Charlotte Renoult  
E-mail: renoulm@coria.fr

CORIA-UMR 6614,  
Normandie Univ, UNIROUEN, INSA Rouen, CNRS, CORIA  
76000 Rouen, France

## 1 Introduction

Atomization designates the fragmentation of a liquid volume into a flow of drops. This fragmentation can have various causes: mechanical, aerodynamic, ultrasonic, electrostatic forces, etc. This diversity has led to several atomizer concepts (Lefebvre and McDonell, 2017). The flow of drops, called a spray, is used in many industrial applications (automotive and aeronautical injection, irrigation, painting, food powder production, etc.) and domestic applications (household products, perfumes, medical inhalers, etc.). The optimization of these applications requires a control of the spray characteristics which can be achieved by a complete knowledge of liquid atomization processes. This objective is challenging because these processes result from many physical mechanism interactions.

Some of the main parameters influencing atomization are the liquid properties. They can be changed by adding a minute amount of flexible polymers with high molecular weight in the liquid. This confers viscoelastic properties to the fluid and affects both atomization processes and drop sizes (Goldin et al., 1972; Gordon et al., 1973; Chao et al., 1984; Mun et al., 1998; Christanti and Walker, 2002; Tirtaatmadja et al., 2006). A quantitative study of these viscoelastic effects on atomization requires precise measurements of the liquid extensional properties, such as the liquid relaxation time or extensional viscosity.

The extensional properties can be measured using an extensional rheometer based on the self-thinning of a liquid filament stretched between two coaxial plates as described in Stelter et al. (2000) and McKinley (2005). This Capillary Breakup Extensional Rheometer (CaBER) consists in analyzing the temporal evolution of the diameter measured at the center of the filament. This

diameter follows two successive thinning regimes: an elasto-capillary regime and a visco-capillary regime. During the elasto-capillary regime, the liquid drainage is controlled by the elastic forces. The thinning dynamic is exponential and scales as  $D(t)/D(0) = \exp(-t/(3t_r))$  where  $D$  is the filament diameter,  $t$  is the time and  $t_r$  is the liquid relaxation time (Entov and Hinch, 1997; Stelster et al., 2000). During the visco-capillary regime, the liquid drainage is controlled by the viscous forces. The thinning dynamic is linear and scales as  $D(t) - D(0) = -\sigma t/\eta_{E,t}$  where  $\sigma$  is the surface tension (between the liquid and the ambient air) and  $\eta_{E,t}$  the terminal extensional viscosity (Stelster et al., 2000).

The CaBER is suitable for polymer solutions whose concentration is high enough such that their shear viscosity is at least ten times larger than the one of water. Note that an elongational rheometer based on the examination of a pulse propagation and widening along a polymeric jet was developed for concentrated solutions (Han et al., 2008). For more dilute polymer solutions, the CaBER rheometer is not reliable because of mechanical (stretching speed limit of the trays and presence of parasitic oscillations) and physical (low relaxation time) constraints (Rodd et al., 2005; Clasen et al., 2012). Even if the CaBER range limits have been extended thanks to the "slow retraction method" (Campo-Deano and Clasen, 2010), the measurement of extensional properties constitutes a known challenge in the case of very dilute polymer solutions (James and Walters, 1993; McKinley, 2005; Larson, 2005; Rodd et al., 2005; Clasen et al., 2012; Sharma et al., 2015).

As an alternative, another method based on jet capillary instability has been known in the literature since the work of Schümmer and Tebel (1983). A jet of viscoelastic liquid is capillary unstable and forms a beads-on-a-string pattern before breaking up. This pattern is composed of quasi-spherical beads and quasi-cylindrical ligaments. The theoretical description of the emergence of this structure in the capillary breakup of dilute polymer solution jets has been formulated by Entov and Yarin (1984) and Yarin (1993). As for the CaBER, the ligament of the beads-on-a-string pattern successively follows an exponential and a linear thinning dynamic and the measurement consists in tracking its diameter over time. In the pioneer work of Schümmer and Tebel (1983), a forced jet experimental setup was used and the ligament diameter was measured on images at several positions along the jet. The relaxation time  $t_r$  was obtained by assuming an elasto-capillary regime and by transposing the spacial variation as a temporal evolution.

In the Rayleigh Ohnesorge Jetting Extensional Rheometry (ROJER) experiments (Keshavarz et al., 2015),

liquid jets excited at a given frequency are used. The high reproducibility of the forced jets coupled with a stroboscopic visualization technique allowed reconstituting temporal evolution of the ligament minimum diameter from which the relaxation time was determined.

The recent work due to Mathues et al. (2018) considered both forced and free jets. This was made possible by using a high-speed visualization technique which provided a real temporal evolution of ligament diameters. They demonstrated that, because of constant axial tension in the jet arising from the constant creation rate of new surface at the nozzle, a faster exponential thinning is observed. The elasto-capillary regime is replaced by an axial-elastic regime that scales as  $D(t)/D(0) = \exp(-t/(2t_r))$ . This dynamics is the same as the one observed for still ligaments of concentrated polymer solutions for which the thinning process is mostly due to gravity (Reneker et al., 2007).

In 2017, a different method to determine the extensional properties from viscoelastic jets was suggested (Tirel et al., 2017). This method makes use of a multi-scale description of the liquid system from which all significant dynamics can be identified. In particular, the dynamic of the ligament thinning and of the bead growing were determined from the evolution of two distinct scales. The main difference between this method and the techniques mentioned above is that the measurements involve the whole visualized liquid system without any prior localization of the center of the ligaments. To this respect, the method is qualified as 'global'. In the application of Tirel et al. (2017), free jets were considered and the analysis was statistic reporting an average description of the ligament thinning mechanism.

The purpose of this paper is to present the theoretical foundation of the multi-scale method and to demonstrate the capability of the statistical approach to return the extensional properties of the polymer solutions. This work is also the opportunity to introduce a new scale more appropriate to extract these properties and to study the influence of a wide range of operating conditions including several nozzle dimensions, jet velocities and solution concentrations. It will also be shown that the method returns the ligament diameter distribution at each position along the jet, and is thus suitable for probing ligament dynamics in more energetic atomization processes.

The theoretical foundation is presented in section 2. The experimental setup and the image processing technique are explained in section 3. Finally, the results are gathered and discussed in section 4.

## 2 Theoretical elements

Consider a system composed of an ensemble of thinning cylinders. All cylinders are subjected to the same thinning process with their lengths kept constant during this process. The cylinder diameters  $D$  are distributed according to the number probability density function  $f_0(D, t)$  which depends on time  $t$ . Characteristic mean diameters  $D_{ab}(t)$  are defined (Mugele and Evans, 1951):

$$(D_{ab}(t))^{a-b} = \frac{\int_0^{+\infty} f_0(x, t) x^a dx}{\int_0^{+\infty} f_0(x, t) x^b dx} \quad (1)$$

where  $a$  and  $b$  are not equal real numbers and  $x$  is the integration variable. For example,  $D_{10}$  is equal to the mean diameter of the distribution  $f_0$ . From the distribution  $f_0(D, t)$ , we define another distribution  $f_1(D, t)$  weighted by the cylinder diameter  $D$  (Dumouchel, 2006):

$$f_1(D, t) = \frac{D}{D_{10}} f_0(D, t) \quad (2)$$

From  $f_n(D, t)$ , the cumulative distributions  $F_n$  can be expressed as follows:  $F_n(D, t) = \int_0^D f_n(x, t) dx$ . The cumulative distributions  $F_0$  and  $F_1$  represent, respectively, the numerical and linear fraction of cylinders whose diameters are inferior to  $D$ .

The system is described by the volume-based scale distribution  $e_3(d, t)$  where  $d$  is the scale of observation (Dumouchel, 2017). This distribution is the ratio of the surface area  $S(d, t)$  of the liquid system having undergone an erosion operation at scale  $d$ , on twice its total volume  $V_T$  :

$$e_3(d, t) = \frac{S(d, t)}{2V_T} \quad (3)$$

For a cylinder, the erosion operation is illustrated in Fig.1: it consists in removing from the cylinder volume the one covered by a spherical element slid along its lateral surface. The erosion operation is applied on each cylinder of the system.

It can be demonstrated that for an ensemble of cylinders whose diameters are distributed according to a distribution  $f_0(D, t)$ , the scale distribution  $e_3(d, t)$  writes (Thiesset et al., 2019):

$$e_3(d, t) = \frac{2}{D_{21}}(1 - F_1(d, t)) - \frac{2d}{D_{20}^2}(1 - F_0(d, t)) \quad (4)$$

The aim in analyzing  $e_3(d, t)$  is to determine a characteristic scale whose dynamics allows retrieving the cylinder diameter dynamics. Such a scale must be a characteristic of the diameter distribution only and not of the erosion operation. Equation (4) reveals that  $e_3(d, t)$  depends on  $d$  by the cylinder diameter distribution (terms

involving  $F_1(D, t)$  and  $F_0(D, t)$  at  $D = d$ ) and on the erosion operation by the coefficient  $-2d/D_{20}^2$  in front of the second term. To get rid of this second dependence,  $e_3(d, t)$  is derived in the scale space and the analysis is conducted on the derivative  $e_3'(d, t)$ :

$$e_3'(d, t) = \frac{de_3(d, t)}{dd} = -\frac{2}{D_{20}^2}(1 - F_0(d, t)) \quad (5)$$

The characteristic scales of the temporal derivative of  $e_3'(d, t)$ , i.e.,  $\dot{e}_3'(d, t)$ , are representative of the cylinder thinning mechanism.  $\dot{e}_3'(d, t)$  is given by:

$$\dot{e}_3'(d, t) = \frac{2}{D_{20}^2} \dot{F}_0(d, t) + \frac{4D_{20}}{D_{20}^3} (1 - F_0(d, t)) \quad (6)$$

where  $\dot{F}_0(d, t)$  and  $\dot{D}_{20}$  designate the temporal derivatives of  $F_0(d, t)$  and  $D_{20}$ , respectively.

As an example, Fig.2 shows the temporal evolution of the function  $\dot{e}_3'(d, t)$  when  $f_0(D, t)$  is taken as a Gaussian distribution, i.e.:

$$f_0(D, t) = \frac{1}{\sigma_f \sqrt{2\pi}} \exp\left(-\frac{(D - D_{10}(t))^2}{2\sigma_f^2}\right) \quad (7)$$

where  $\sigma_f$  is the distribution standard deviation. Figure 2 exhibits two characteristic scales:  $d_1(t)$  and  $d_4(t)$ . The scale  $d_1(t)$  is the smallest one for which  $\dot{e}_3'(d, t) = 0$ . This scale used to be considered to measure the relaxation time (Tirel et al., 2017). However, its determination was found tricky at the beginning of the ligament thinning process where  $\dot{e}_3'(d, t)$  for  $d < d_1$  is close to zero. The scale  $d_4(t)$  is the one for which  $\dot{e}_3'(d, t)$  is a maximum. Its determination is easier than the one of  $d_1(t)$ . Within the scope of this work, it is decided to investigate the cylinder diameter dynamics on the basis of the scale  $d_4$ . This scale satisfies the following equation:

$$\begin{aligned} \dot{e}_3''(d_4, t) &= \frac{d\dot{e}_3'(d_4, t)}{dd} = 0 \\ &= \frac{2}{D_{20}^2} \left. \frac{d\dot{F}_0(d, t)}{dd} \right|_{d=d_4} - \frac{4\dot{D}_{20}}{D_{20}^3} f_0(d_4, t) \end{aligned} \quad (8)$$

The dynamic of  $d_4(t)$  is investigated for two cylinder diameter thinning regimes, i.e., an exponential thinning and a linear thinning.

### Exponential thinning regime

In this regime, the cylinders are subjected to an identical exponential thinning:

$$D(t) = D(0) e^{-\alpha t} \quad (9)$$

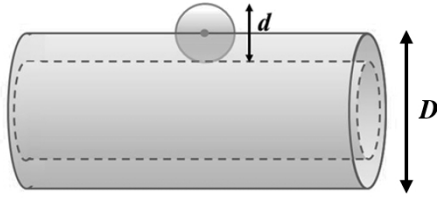


**Fig. 1** Erosion operation at scale  $d$  of a cylinder of diameter  $D$ .

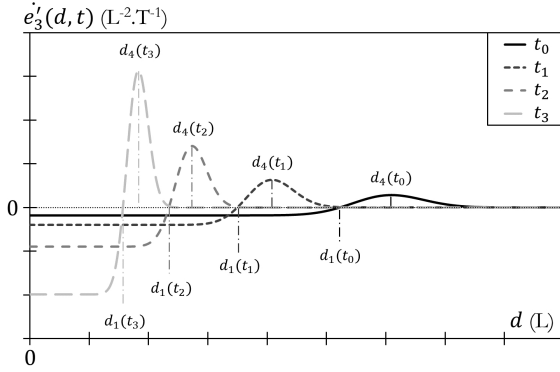


**Fig. 2**  $\dot{e}'_3(d, t)$  versus  $d$  for an ensemble of thinning cylinders whose diameters are distributed according to a Gaussian distribution.  $t_0 < t_1 < t_2 < t_3$ ,  $D_{10} = 15$  and  $\sigma_f = 1.5$  at  $t_0$  (arbitrary length and time).

where  $\alpha$  is a positive real number. By switching the integrals from Eq.(1) into infinite Riemann sums, the mean diameters  $D_{ab}$  can be expressed as:

$$D_{ab}(t) = D_{ab}(0) e^{-\alpha t} \quad (10)$$

Thus, the temporal derivative  $\dot{D}_{20}$  is equal to:

$$\dot{D}_{20}(t) = -\alpha D_{20}(t) \quad (11)$$

Moreover, it can be shown that:

$$\dot{F}_0(d, t) = \left[ -f_0(D) \dot{D} \right]_{D=d} \quad (12)$$

Using Eqs.(9), (10), (11) and (12), Eq.(8) writes:

$$\dot{e}_3''(d_4, t) = \frac{2\alpha}{D_{20}^2} (d_4 f_0'(d_4, t) + 3f_0(d_4, t)) = 0 \quad (13)$$

This leads to an implicit expression of the scale  $d_4(t)$ :

$$d_4(t) = \frac{-3f_0(d_4, t)}{f_0'(d_4, t)} \quad (14)$$

It can be shown that the scale  $d_4(t)$  given by Eq.(14) corresponds to the diameter for which the function  $D^3 f_0(D, t)$  exhibits a maximum. As observed by Dumouchel (2006), this diameter is a mean diameter. In virtue of Eq.(10),

$d_4(t)$  has therefore the same thinning dynamic as the cylinder diameters, i.e.:

$$d_4(t) = d_4(0) e^{-\alpha t} \quad (15)$$

Thus, the ligament deformation rate  $\dot{\epsilon}$  and the apparent elongational viscosity  $\eta_{E,app}$  (Stelter et al., 2000; McKinley, 2005) can be calculated using  $d_4(t)$ :

$$\dot{\epsilon}(t) = \frac{-2\dot{D}_{10}(t)}{D_{10}(t)} = \frac{-2\dot{d}_4(t)}{d_4(t)} \quad (16)$$

$$\eta_{E,app}(t) = \frac{2\sigma}{\dot{\epsilon}(t)D_{10}(t)} = \frac{-\sigma}{\dot{d}_4(t)} \quad (17)$$

In this regime,  $\dot{\epsilon}$  is constant (Stelter et al., 2000; McKinley, 2005) and equal to  $2\alpha$  and  $\eta_{E,app}$  increases exponentially. If the regime is an axial-elastic one (Mathues et al., 2018),  $\alpha$  is linked to the liquid relaxation time  $t_r$  according to:  $\alpha = 1/(2t_r)$ , and  $t_r$  is deduced from Eq.(16) as follows:

$$t_r = \frac{1}{\dot{\epsilon}} \quad (18)$$

### Linear thinning regime

In this regime, the cylinders are subjected to a linear thinning:

$$D(t) = D(0) - \beta t \quad (19)$$

with  $\beta$  a constant positive real number. According to Eq.(1), it can be shown that:

$$\dot{D}_{20}(t) = -\beta \frac{D_{10}(t)}{D_{20}(t)} \quad (20)$$

$$\dot{F}_0(d, t) = -\beta f_0(d, t) \quad (21)$$

In this case, Eq.(8) gives:

$$\dot{e}_3''(d_4, t) = \frac{2\beta}{D_{20}^2} \left( f_0'(d_4, t) + \frac{2}{D_{21}} f_0(d_4, t) \right) \quad (22)$$

$d_4(t)$  is solution of the implicit equation:

$$D_{21} f_0'(d_4, t) + 2f_0(d_4, t) = 0 \quad (23)$$

Contrary to the previous case, solving Eq.(23) is not straightforward. To ease the problem,  $f_0(D, t)$  is considered as a Gaussian distribution (Eq.(7)). In this linear thinning regime, it is appropriate to consider  $\sigma_f$  independent of time. This leads to the following expression

$$d_4(t) = D_{10}(t) + 2\sigma_f^2/D_{21}(t) \quad (24)$$

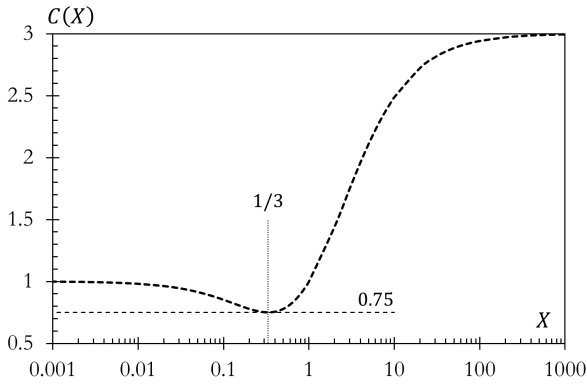


**Fig. 3** Proportional coefficient  $C(X)$ .

Considering that  $\sigma_f^2 = D_{20}^2(t) - D_{10}^2(t)$  (Sowa, 1992), it can be shown that:

$$\begin{aligned} \dot{d}_4(t) &= \dot{D}_{10}(t) \left( 1 + \frac{2X(X-1)}{(1+X)^2} \right) \\ &= \dot{D}_{10}(t)C(X) = -\beta C(X) \end{aligned} \quad (25)$$

where  $X = (\sigma_f/D_{10})^2$ . Eq.(25) expresses the fact that the dynamic of the scale  $d_4$  is not equal to the thinning dynamic of the cylinders but is proportional to it. The coefficient of proportionality  $C(X)$  depends on the relative width of the cylinder diameter distribution  $X$ . This dependency, illustrated in Fig.3, shows that the dynamic of  $d_4(t)$  is the same as the cylinder diameter when the distribution is narrow and that it can be three times higher for larger distributions. The relative width  $X$  can be determined from the distribution  $f_0(D)$ , which, according to Eq.(5), is given by:

$$f_0(d, t) = \frac{D_{20}^2}{2} e_3''(d, t) \quad (26)$$

Using Eq.(16), the ligament deformation rate  $\dot{\varepsilon}$  becomes:

$$\begin{aligned} \dot{\varepsilon}(t) &= \frac{-2\dot{D}_{10}(t)}{D_{10}(t)} = \frac{-2\dot{d}_4(t)}{d_4(t)} \left( 1 + \frac{4X}{3X^2 + 1} \right) \\ &= \frac{-2\dot{d}_4(t)}{d_4(t)} C_{\dot{\varepsilon}}(X) \end{aligned} \quad (27)$$

In this regime,  $\eta_{E,app}(t)$  is constant and equal to the liquid terminal extensional viscosity  $\eta_{E,t}$  (Stelter et al., 2000; McKinley, 2005):

$$\eta_{E,t} = \frac{2\sigma}{\dot{\varepsilon}(t)D_{10}(t)} = \frac{-\sigma C(X)}{\dot{d}_4(t)} = \frac{\sigma}{\beta} \quad (28)$$

### 3 Experimental method

#### 3.1 Jet imaging setup

The experimental setup used to produce images of vertical free liquid jets is presented in Fig.4. It is composed of two parts: the hydraulic system and the optical visualization system.

The hydraulic part comprises a syringe-pump, a supplying tube and an injector. The syringe-pump (Chemyx Nexus 6000) has four 50 ml syringes that are connected in parallel to the supplying tube. The injector is a cylindrical body (5 mm internal diameter and 85 mm length) ended by a nozzle. The nozzle is a thin cylindrical plate with a cylindrical hole in its center. The syringe pump, supplying tube and injector are installed at the same height to limit pressure changes.

The optical visualization system is a backlight imaging assembly. It comprises a light source, a telescopic sight and a camera. The light source is a CAVITAR laser source (Cavilux Smart 400W) with its optical fiber and 25 mm collimation optics. It is a monochromatic pulsed source around 640 nm and weakly coherent. The telescopic sight is a long-distance microscope (Infinity K2 DistaMax). The camera sensor has 29 million pixels (HR29050 model from SVS-Vistek) and its minimum exposure time is equal to 17  $\mu$ s. It returns 8-bit grayscale images in TIFF format without compression using the acquisition software StreamPix6. The camera sensor exposure and the light source are synchronized by a TTL signal generator. The image frame rate is set at 2 Hz. The duration of the light pulse is chosen equal to 20 ns to freeze the jet on the image. A moving object is frozen when its displacement during the light exposure is lower than the image resolution. The finest resolution of the optical system is 0.56  $\mu$ m/pixel, that allows a maximal jet velocity of 28 m/s for the chosen light exposure.

For the chosen image resolutions, the field of view is not large enough to visualize the jet entirely from the nozzle to the breakup region. The injector is placed vertically on a displacement system (200 mm vertical rise, ZABER T-LSM 3-D system) allowing the jet to be focused and visualized at different vertical positions under the injector without modifying the optical visualization system. A number of 150 images are taken for each vertical position. An example of reconstructed jet is visible in Fig.5, showing the different jet positions. The injector is placed in a containment chamber to protect the jet from ambient air draft.

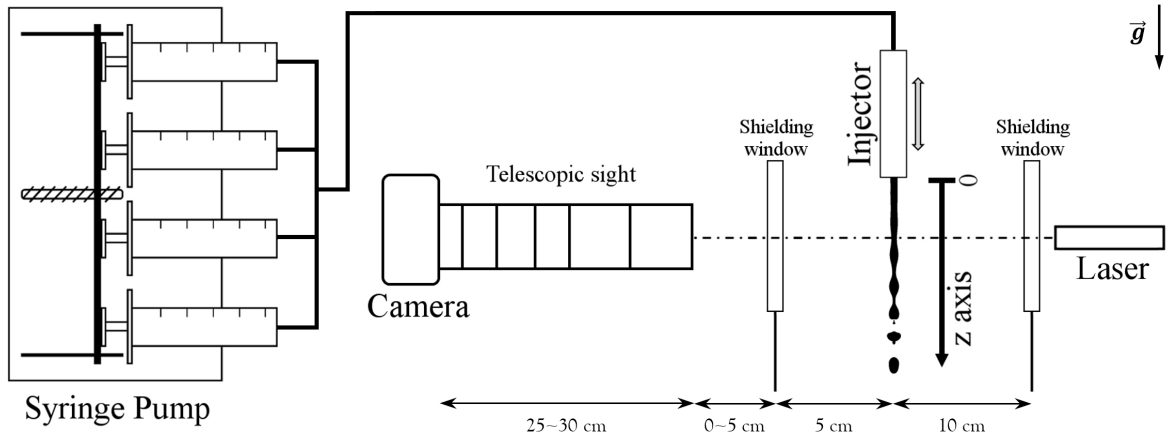


Fig. 4 Free jet experimental setup.

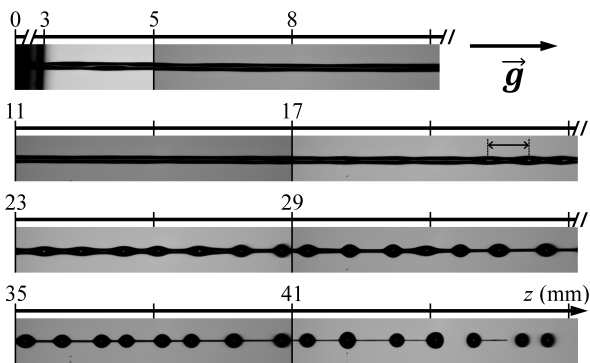


Fig. 5 Reconstructed viscoelastic liquid jet.

### 3.2 From raw image to EDM image

The captured raw images present dark objects that represent the liquid phase on bright background as can be seen in Fig.6a. The image processing is performed with a self-written algorithm based on the Fourier formalism and the concept of the point spread function (Blaisot and Yon, 2005; Fdida and Blaisot, 2009; Blaisot, 2012). It consists in three steps illustrated in Fig.6. The first step deletes the background inhomogeneities as presented in Fig.6b. The second step segments the image in a two-level image as shown in Fig.6c. This step is divided in two parts. An object detection part, based on a combination of intensity threshold plus wavelet transform, identifies the objects on the image (Yon, 2003). Then, the segmentation part is performed to each object with a local intensity threshold using the point spread function concept. The third step calculates the image Euclidian Distance Map (EDM), as presented in Fig.6d. For each pixel of the jet, this step attributes a gray level value corresponding to its distance from the closest object interface.

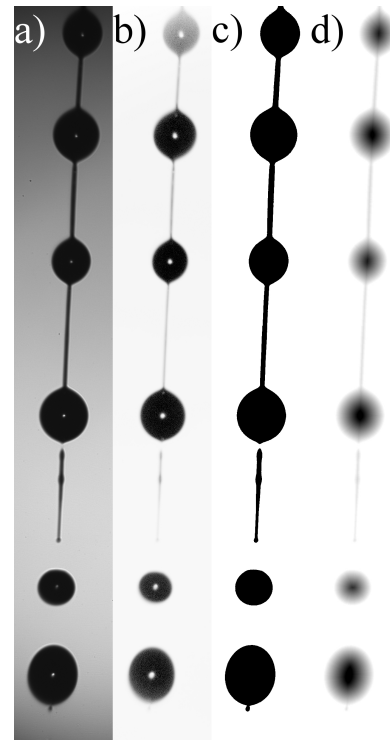


Fig. 6 Image processing steps. a) Raw image. b) Normalized image. c) Segmented image. d) EDM image.

### 3.3 From EDM images to scale distribution

With the use of the software ImageJ (Schneider et al., 2012) and the EDM images, the volume-based scale distribution  $e_{3_i}(d, z)$  is calculated on the image  $i$  for a portion of the jet image delimited by an analyzing window centered at position  $z$  where the  $z$ -axis is directed downstream with the origin at the nozzle exit (Fig.4). Although images provide a 2D information, the 3D scale distribution  $e_{3_i}(d, z)$  is deduced by assuming

the axisymmetry of the liquid jet from the 2D images (Dumouchel et al., 2017). This hypothesis is acceptable due to the axisymmetric nature of the capillary instability mechanism. The height  $H_w$  of the analyzing window is taken of the order of the naturally selected perturbation wavelength. This corresponds to a compromise between localness and number of images required to have a converged average scale distribution. The local scale distribution  $e_3(d, z)$  is deduced from the scale distribution on each image  $e_{3_i}(d, z)$  as follows:

$$e_3(d, z) = \sum_{i=1}^m \frac{V_{T_i}}{\sum_{j=1}^m V_{T_j}} e_{3_i}(d, z) \quad (29)$$

with  $V_{T_i}$  the jet volume in the analyzing window on image  $i$ . Then, the spatial  $z$  dependence of the scale distribution is transformed as a temporal  $t$  dependence from the hourly equation of a free-falling object with a velocity  $V_{jet}$ . The equivalent time  $t$  is therefore defined by:

$$t = \frac{\sqrt{V_{jet}^2 + 2gz} - V_{jet}}{g} \quad (30)$$

where  $g$  is the gravitational acceleration and  $V_{jet}$  the mean jet velocity.  $V_{jet}$  is defined from the jet flow rate (measured by weighting the collected liquid drops during a measured time period) and the jet diameter  $D_{jet}$  (measured on the jet undisturbed part). When  $V_{jet}^2 \gg 2gz$  the gravity force on the jet becomes negligible and Eq.(30) simplifies as  $t = z/V_{jet}$ .

To get the temporal evolution of the jet scale distribution  $e_3(d, t)$ , the analyzing window is successively shifted along the jet. This shift  $\Delta H_w$  is chosen equal to  $H_w$  or  $H_w/2$ , depending on the jet operating conditions.

### 3.4 From scale distribution to liquid extensional properties

The function  $e'_3(d, t)$  is calculated from the scale distribution  $e_3(d, t)$ . An example of  $e'_3(d, t)$  is presented in Fig.7. Comparing Fig.7 with Fig.2 shows that the BOAS reports negative values. They are due to the presence of the beads. This behavior is similar to that reported for Newtonian ligaments (Dumouchel et al., 2017). As shown in Fig.7,  $e'_3(d, t)$  allows to identify the scale  $d_4(t)$ . The figure shows also the scale  $d_{max}(t)$  which is defined as the minimum scale for which  $e_3(d, t)$  is equal to zero.  $d_{max}(t)$  is set as the minimum scale for which  $e_3(d, t) < 0.5\% e_3(0, t)$ .

The temporal evolution of  $d_4(t)$  is presented in Fig.8. As expected, this scale decreases with time according to the successive thinning regimes followed by ligaments.

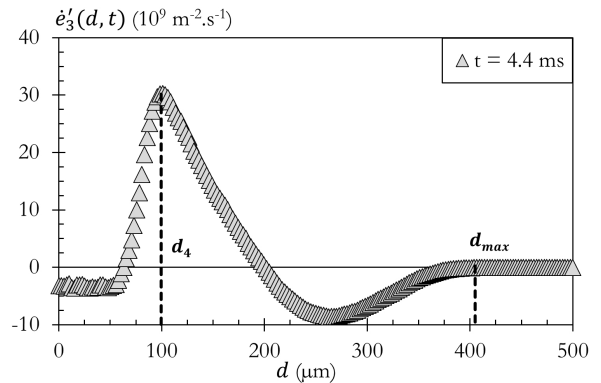


**Fig. 7** Scale distribution  $e'_3(d, t)$  plus  $d_4(t)$  measurement. Solution 5 ppm, nozzle B3,  $Q_v = 23.7 \cdot 10^{-8} \text{ m}^3/\text{s}$  (see section 4.1).

The calculations of  $\dot{\epsilon}$  and  $\eta_{E,app}$  requires the temporal derivative  $\dot{d}_4(t)$ . Calculating this derivative necessitates a prior fit of  $d_4(t)$ . This fit is performed with the Locally Weighted Scatterplot Smoother implemented in SigmaPlot (version 11.0) under the name LOESS. The example of data fitting presented in Fig.8 shows that this method is well adapted.

Figure 9 shows an example of the temporal evolution of  $-2\dot{d}_4(t)/d_4(t)$  and of  $-\sigma/\dot{d}_4(t)$ . After a first increase,  $-2\dot{d}_4(t)/d_4(t)$  reaches a constant value. As explained in Section 2, this behavior is a characteristic of an exponential thinning regime of the ligaments. If this regime is an axial-elastic one, the relaxation time  $t_r$  can be determined from Eqs.(16) and (18). During this regime,  $-\sigma/\dot{d}_4(t)$  increases with time as expected. (The initial decrease of this function has no physical sense: it associates the exponential decrease of the jet troughs with a decrease of a viscosity.) After the exponential thinning regime,  $-2\dot{d}_4(t)/d_4(t)$  increases again while  $-\sigma/\dot{d}_4(t)$  becomes rather constant. This expected behavior is a characteristic of the visco-capillary regime from which the terminal extensional viscosity can be measured. The slight increase of  $-\sigma/\dot{d}_4(t)$  is due to the variation of the dynamic of  $d_4(t)$  during this regime as expressed by Eq.(25). We note here that this temporal variation remains weak. The terminal extensional viscosity is measured with the first value of the visco-capillary regime. Equation (28) is used for this purpose where  $C(X)$  is determined from Fig.3 with  $X$  being obtained from the function  $e''_3(d, t)$  as explained in section 2.

### 3.5 Other measurements

The Rayleigh jet regime and free jet nature hypotheses need to be verified. For this purpose the jet stability curve is measured (Goldin et al., 1969, 1972; Mun et al.,

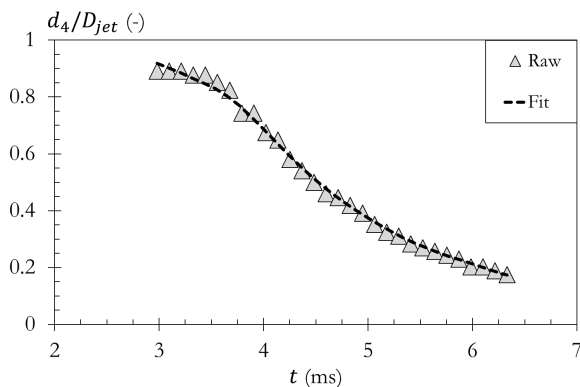


**Fig. 8** Dimensionless scale  $d_4/D_{jet}$  temporal evolution and fitting. Solution 5 ppm, nozzle B3,  $Q_v = 23.7 \cdot 10^{-8} \text{ m}^3/\text{s}$  (see section 4.1).

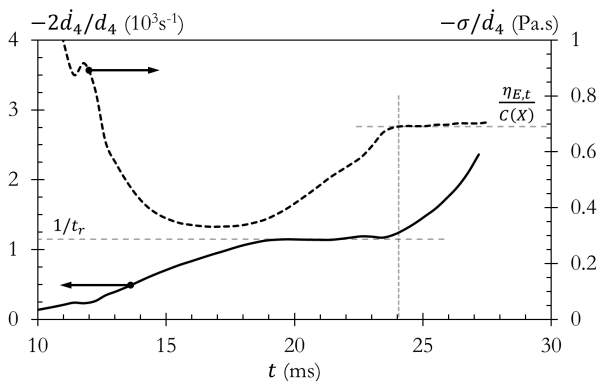


**Fig. 9** Apparent extensional viscosity  $\eta_{E,app}$  as function of the ligament deformation rate  $\dot{\epsilon}$ . Solution 5ppm, nozzle B5,  $Q_v = 45.2 \cdot 10^{-8} \text{ m}^3/\text{s}$  (see section 4.1).

1998) as well as the growth rate and wave number of the initial jet instability.

The jet stability curve is by definition the breakup length as function of the jet velocity. The breakup length  $L_{BU}$  is defined as the distance between the nozzle exit and the jet breakup point. The jet breakup point is the point for which the liquid jet is no longer continuous on the segmented images. The breakup length varies in time for a free liquid jet, leading to a breakup length distribution. The mean breakup length  $\bar{L}_{BU}$  is extracted from this distribution and used as the breakup length estimator for the jet stability curve.

The dimensionless temporal growth rate  $\omega$  of the jet instability is related to the temporal evolution of the diameter of the jet crests, this diameter being equal to the maximum scale  $d_{max}(t)$ :

$$\frac{d_{max}(t)}{D_{jet}} - 1 \propto \exp\left(\omega \frac{t}{t_\sigma}\right) \quad (31)$$

where  $t_\sigma = \sqrt{\rho D_{jet}^3 / \sigma}$  is the capillary time. Thus,  $\omega$  is determined by following the exponential temporal evolution of  $d_{max}(t)$  as explained in previous works (Dumouchel et al., 2017; Tirel et al., 2017).

The dimensionless free jet wave number  $\bar{k}$  is determined using the same protocol as Charpentier et al. (2017). The jet contours are extracted from the segmented images corresponding to the linear regime of the instability (previously identified on  $d_{max}(t)$  behavior). From these contours, the distances between successive maxima on the jet surface are measured, and a distribution of wave lengths is deduced. The dimensionless free jet wave number is defined as the inverse of the mean wave length  $\bar{\lambda}$  of the distribution:  $\bar{k} = \pi D_{jet} / \bar{\lambda}$ .

## 4 Application

### 4.1 Fluids, nozzles and flow rates

Free falling jet experiments are performed for different viscoelastic fluids, nozzle geometries and flow rates.

The viscoelastic fluids are dilute polymer solutions with different polymer concentration. The used polymer is the Poly(ethylene oxide) (PEO) with an average molar mass  $M_w = 8 \cdot 10^3 \text{ kg/mol}$  according to Sigma-Aldrich. The polymer is dissolved into demineralized water with 5% in mass of isopropyl alcohol. The isopropyl alcohol fraction facilitates the dispersion of the PEO powder in the water (Charpentier et al., 2017). Six different concentrations are prepared from 5 to 20 part per million (ppm) in mass of PEO. The solution shear viscosity and density are measured with the STABINGER SVM 3000 viscometer and the surface tension with the LAUDA TVT2 tensiometer (dripping drop volume measurement) at  $T = 20^\circ\text{C}$ . These fluid properties are closed to those of the solvent (less than 5 % for the shear viscosity and less than 1 % for density and surface tension): density  $\rho = 989 \text{ kg/m}^3$ ; shear viscosity  $\mu = 1.34 \text{ mPa.s}$ ; surface tension  $\sigma = 48.9 \text{ mN/m}$ .

Seven nozzles are used (see table 1). The inner diameter  $D_{in}$ , the outer diameters  $D_{or}$  and length  $L_{or}$  are measured in order to check the cylindrical shape of each nozzle. From images of the holes taken with a microscope, an equivalent-surface diameter is calculated. As shown in table 1, the nozzles are not perfectly cylindrical:  $D_{in}$  is never equal to  $D_{or}$ . In the following, the larger diameter is chosen as the liquid entry of the nozzle. The Ohnesorge number based on  $D_{or}$  ranges from  $8 \cdot 10^{-3}$  to  $18 \cdot 10^{-3}$ . For each couple solution-nozzle, the flow rate is varied in the domain  $Q_v \in [1.82; 47.5] \cdot 10^{-8} \text{ m}^3/\text{s}$ . All experiment data are presented in table 2.

**Table 1** Nozzle dimensions in  $\mu m$ .

Ref	B1	B2	B3	B4	B5	B6	B7
$D_{in}$	47	116	214	373	618	528	557
$D_{or}$	42	105	200	367	480	500	500
$L_{or}$	300	300	300	1000	1000	1000	5000

The image resolutions are chosen so that the diameter of the cylindrical jet in its undisturbed part is displayed over at least 80 pixels. Such a criterion allows to apply the multi-scale analysis without sub-pixel segmentation. To respect this criterion, different resolutions and visual fields were used depending on the nozzle diameter, as referenced in table 3.

#### 4.2 Nature of liquid jet experiments

The jet stability curve  $\bar{L}_{BU}$  versus  $V_{jet}$  for different solution-nozzle couples is shown in Fig.10. The error bar on each data point is equal to twice the standard deviation of the Gaussian fit of the breakup length distribution. This latter is shown on the figure inset for a particular data point.

A linear increase of  $\bar{L}_{BU}$  is observed for each case, indicating that the experiments lie in the jet Rayleigh regime. For the 20 ppm solution, the stability curve reaches a plateau from the three highest jet velocities. This breakup length saturation was previously observed in the experiments of Goldin et al. (1972) and Mun et al. (1998) for dilute polymer solutions, contrary to the Newtonian case. To our knowledge, this behavior has not yet been interpreted.

The dimensionless growth rate  $\omega$  versus the dimensionless wave number  $\bar{k}$  is presented in Fig.11. The results are concentrated around the most unstable wave number predicted by linear stability theory of Rayleigh (Rayleigh, 1878; Middleman, 1965; Bousfield et al., 1986) whose application is authorized by the small Ohnesorge numbers of the jets:  $\bar{k} = 0.69$  and  $\omega = 0.34$ . This curve confirms the free nature of the liquid jet experiments.

#### 4.3 Extensional property measurements

The operating conditions of this work are close to those of Mathues et al. (2018) except for the polymer concentrations which are less here. It seems appropriate to consider that the exponential thinning of the present jet ligaments is axial-elastic. Therefore, the relaxation time  $t_r$  is obtained from Eqs. (16) and (18).

Table 2 gathers the relaxation times and the terminal extensional viscosities. Note that for some cases, the relaxation time is not reported. For these cases, the

**Table 2** Experiment operating condition list and results of extensional properties results.

$c$ $\pm 1\%$ (ppm)	Nozzle	$Q_v$ $\pm 1\%$ ( $10^{-8} \text{ m}^3/\text{s}$ )	$D_{jet}$ $\pm 3\%$ ( $\mu\text{m}$ )	$V_{jet}$ $\pm 5\%$ (m/s)	$t_r$ $\pm 10\%$ (ms)	$\eta_{E,t}$ $\pm 10\%$ (Pa.s)
5	B1	1.82	46.0	10.9	-	0.41
		2.57	47.0	14.8	0.066	0.32
		2.92	47.0	16.8	0.072	0.36
		3.53	46.0	21.2	0.074	0.32
		3.93	47.0	22.7	0.057	0.44
		4.23	46.5	24.9	0.050	0.37
5	B2	4.53	46.5	26.7	0.036	0.26
		2.92	125	2.37	-	3.0
		4.53	121	3.94	0.74	1.8
		6.55	117	6.09	0.56	1.6
		8.47	114	8.29	0.32	1.3
		11.7	112	11.9	-	0.95
5	B3	14.5	112	14.8	0.23	0.80
		17.0	112	17.3	-	0.84
		5.93	195	1.99	-	3.2
		9.17	190	3.23	-	2.6
		13.3	185	4.94	1.3	2.8
		17.2	184	6.46	0.90	2.2
5	B4	20.3	200	6.49	1.1	2.3
		23.7	187	8.61	0.72	2.1
		28.8	190	10.2	-	1.3
		34.7	339	3.85	2.1	2.5
		45.2	484	2.46	4.1	2.8
		36.7	549	1.55	6.6	7.7
5	B5	42.2	539	1.85	5.4	4.1
		47.5	534	2.12	4.8	3.4
		36.7	488	1.97	9.5	4.4
5	B6	47.5	463	2.82	8.4	4.5
		2.62	133	1.88	-	7.5
7.5	B2	4.22	127	3.33	1.4	3.2
		5.93	119	5.34	0.74	2.1
		8.42	117	7.83	0.54	2.0
		11.8	114	11.5	0.35	1.2
		13.8	113	13.7	0.35	1.2
		16.8	114	16.6	-	1.00
		3.42	138	2.29	-	6.0
10	B2	4.65	129	3.56	-	6.1
		6.53	122	5.59	0.93	3.8
		8.45	119	7.60	0.65	2.4
		11.7	117	10.9	0.47	1.1
		14.4	115	13.9	-	1.2
		15.6	113	15.6	-	1.7
12.5	B2	2.92	134	2.07	3.3	8.3
		4.73	127	3.74	1.5	4.7
		6.45	122	5.52	1.1	3.3
		8.68	119	7.80	0.68	2.1
		11.3	117	10.5	0.51	2.4
		14.4	115	13.9	-	2.1
		17.5	114	15.6	-	0.91
15	B2	2.92	140	1.89	3.0	8.4
		4.73	127	3.74	1.7	4.3
		6.57	121	5.70	0.90	3.0
		8.57	111	8.85	0.60	2.4
		11.6	115	11.2	0.59	2.2
		14.5	113	14.4	0.45	1.6
20	B2	17.3	112	17.6	-	1.7
		2.92	141	1.87	-	12
		4.73	130	3.56	2.9	7.6
		6.55	124	5.43	1.5	5.3
		8.47	121	7.36	1.4	4.1
		11.7	117	10.9	0.83	3.3
14.3	114	14.0	-	2.7		

**Table 3** Field of view  $FV$  (mm<sup>2</sup>) and image resolution  $IR$  (px/mm) used with the different nozzles.

Ref	B1, B2	B2 (20ppm)	B3	B4, B5, B6, B7
$FV$	3.68*2.46	4.84*3.22	8.29*5.52	11.0*7.31
$IR$	1780	1380	792	600

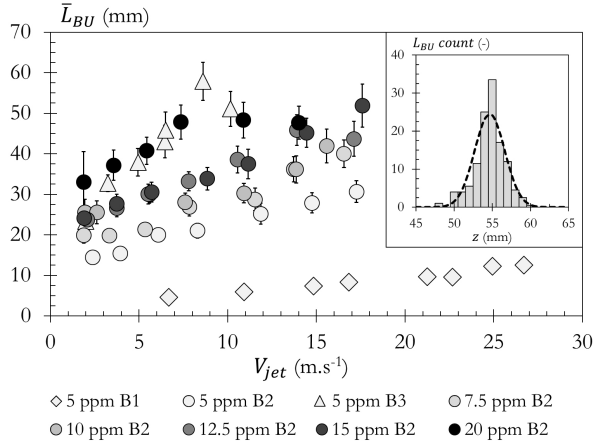


**Fig. 10** Jet stability curves. The inset figure shows an example of breakup length distribution (bar chart) and its Gaussian fit (dash line), case 5 ppm B3 at  $V_{jet} = 8.61$  m/s and  $\bar{L}_{BU} = 57.9$  mm.

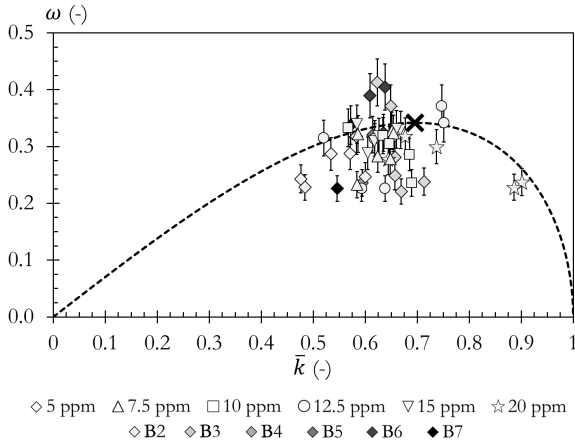


**Fig. 11** Dimensionless growth rate  $\omega$  as function of the dimensionless selected wave number  $\bar{k}$ . Dash line: prediction of the Rayleigh linear theory. Cross: the most unstable wave number.

temporal evolution of the function  $-2\dot{d}_4/d_4$  did not report any plateau and no exponential thinning regime could be identified.

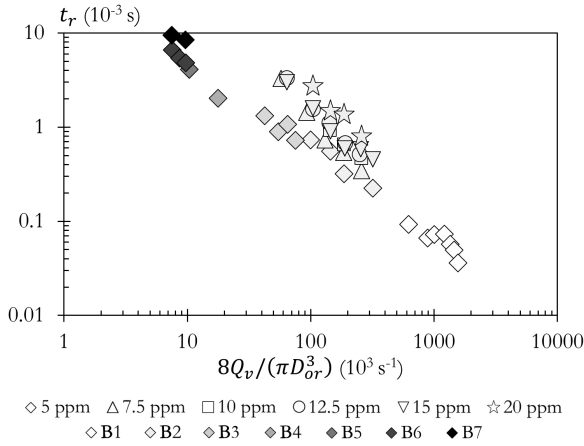
The relaxation times  $t_r$  show a dependence with the mean jet velocity  $V_{jet}$  and with the injection nozzle diameter. For example, the 7.5 ppm solution has a  $t_r$  equal to 0.23 ms for  $V_{jet} = 13.7$  m/s which is four times lower than the  $t_r$  (0.96 ms) measured for

$V_{jet} = 3.33$  m/s. Figure 12 presents the relaxation time  $t_r$  as a function of an equivalent deformation rate in the injector. This deformation rate is evaluated as the ratio of the velocity in the orifice  $V_{or}$  to the orifice radius:  $2V_{or}/D_{or} = 8Q_v/(\pi D_{or}^3)$ . A strong power law correlation is observed. The exponent of this law appears to be a function of the concentration. The behavior shown in Fig.12 suggests that there is a modification of the solution extensional properties during the liquid injection phase.

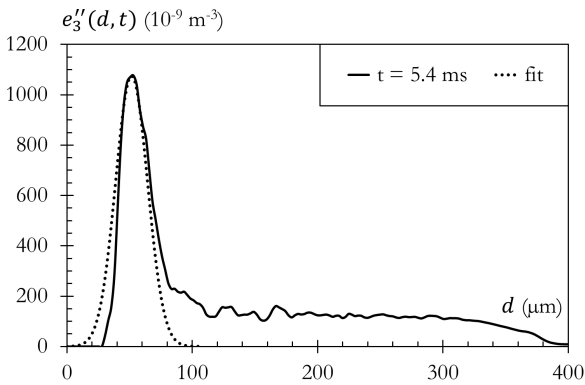
A degradation mechanism of polymeric solutions due to high deformation rates in injectors has been reported in several studies (Merrill and Leopairat, 1980; Nguyen and Kausch, 1988). It has been shown that the polymer solution presents a critical deformation rate above which polymers break (Merrill and Leopairat, 1980). In addition, increasing the deformation rate above this critical value increases the polymer scission rate. The mutual influence of mechanical degradation, rheological behavior and flow of polymeric liquids has been theoretically established by Yarin (1991). The mechanical degradation leads to a decrease of polymer molecular weight which, according to the Zimm model (Bird et al., 1987), must be accompanied by a reduction of the solution relaxation time. As in Stelter et al. (2002a) and Stelter et al. (2002b) experimental works, the degradation may be caused by liquid injection. In this case, the decrease of relaxation time correlates with the increase of the injection velocity as observed in Fig.12. Therefore, the behavior reported in this figure is clearly related to the presence of mechanical degradation which, considering the high molecular weight of the polymer, could have been expected (Stelter et al., 2002a). These results are meliorative for the analyzing method.

Figure 13 presents an example of  $e_3''(d, t)$  at an early stage of the visco-capillary regime.  $e_3''(d, t)$  presents two parts: a peak at low scales, followed by a constant plateau at large scales. The peak represents the ligament diameter distribution (see Eq.(5)) and the plateau represents the bead structures. As shown by the dash line, the Gaussian distribution is a satisfactory fit of the ligament diameter distribution. The same quality is obtained for all experiments. The mean value and the standard deviation of the Gaussian fit are measured, leading to coefficients  $X$  (Eq. (25)) in the range [0.02; 0.04] for all experiments at the starting time of the visco-capillary regime. This corresponds to a correcting coefficient  $C(X)$  ranging in the interval [0.93; 0.96]. These values of  $C(X)$  are close to 1, allowing neglecting the correction in the measurement of the terminal extensional viscosity  $\eta_{E,t}$  (see Eq. (28)).

Figure 14 shows  $\eta_{E,t}$  as a function of  $t_r$ . A very strong correlation between these two quantities is ob-



**Fig. 12** Relaxation time  $t_r$  as function of the nozzle deformation rate  $8Q_v/(\pi D_{or}^3)$ .



**Fig. 13**  $e_3''(d, t)$  during the visco-capillary regime. Dotted line is the Gaussian fit of ligament diameter distribution. Solution 5 ppm, nozzle B3,  $Q_v = 23.7 \cdot 10^{-8} \text{ m}^3/\text{s}$ .

served. This correlation extends the experimental correlation obtained by Stelter et al. (2002a,b) (crosses in Fig.14). Therefore, Stelter et al. (2002a) empirical model for flexible polymer macromolecules as PEO (dash line in Fig.(5)) appears very appropriate for the present results even if the model was obtained in a completely different range of operating conditions. The model of Stelter et al. (2002a) therefore appears very robust.

## 5 Conclusion

A statistical and multi-scale method for measuring the extensional properties of viscoelastic solutions during free jet atomization has been demonstrated. In particular, the characteristic scale  $d_4(t)$  has been introduced and the capability of determining the relaxation time and the terminal extensional viscosity of the solution from its temporal evolution has been demonstrated. Furthermore, it has been shown that the diameter dis-

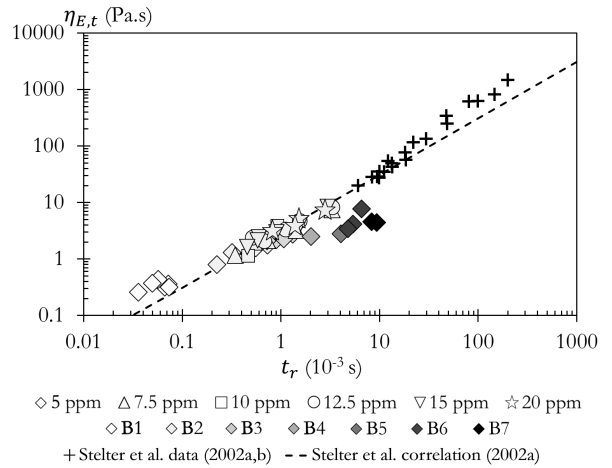


**Fig. 14** Terminal extensional viscosity  $\eta_{E,t}$  as function of relaxation time  $t_r$ . Comparison with Stelter et al. experimental results (2002a,b) and Stelter et al. correlation (2002a):  $\eta_{E,t} = 3074.9t_r + 0.003$ .

tribution of the BOAS ligaments seen along the jet can be obtained.

This method is applied on free jets of viscoelastic liquids with several polymer concentrations, flow rates and nozzle geometries. The free nature of the jet has been checked from the jet stability curve, the perturbation wave number and corresponding growth rate. The results show that the relaxation time  $t_r$  is a function of an equivalent deformation rate in the nozzle due to polymer mechanical degradation during injection.

A strong correlation between the terminal extensional viscosity and the relaxation time is observed. It occurs that this correlation is in good agreement with the empirical model established by Stelter et al. (2002b).

These results validate the method. Although it could be applied with any polymer solutions, it is advised to reserve it for dilute solutions only. Concentrated solutions would produce long jets that would be pejorative for the compactness of the experiment. This work can be adapted to probe the ligaments appearing in more energetic atomization processes offering a direct way to reach their size and extensional property distributions. This is precisely what we intend to do next.

**Acknowledgements** The authors acknowledge both Jean-Baptiste Charpentier for the jet wave number measurement implementation from its own work (Charpentier et al., 2017) and Massinissa Saadi for its contribution to jet experiment acquisitions.

The authors also acknowledge the financial support from the French National Research Agency (ANR) through the program Investissement d'Avenir (ANR-10 LABX-09-01), LABEX EMC3

## References

- Bird RB, Armstrong RC, Hassager O (1987) Dynamics of polymeric liquids. Vol. 1: Fluid mechanics. John Wiley and Sons Inc
- Blaisot JB (2012) Drop size and drop size distribution measurements by image analysis. Heidelberg, Germany
- Blaisot JB, Yon J (2005) Droplet size and morphology characterization for dense sprays by image processing: application to the diesel spray. *Experiments in fluids* 39(6):977–994
- Bousfield DW, Keunings R, Marrucci G, Denn MM (1986) Nonlinear analysis of the surface tension driven breakup of viscoelastic filaments. *Journal of Non-Newtonian Fluid Mechanics* 21(1):79–97
- Campo-Deano L, Clasen C (2010) The slow retraction method (srm) for the determination of ultra-short relaxation times in capillary breakup extensional rheometry experiments. *Journal of Non-Newtonian Fluid Mechanics* 165(23–24):1688–1699
- Chao KK, Child CA, Grens EA, Williams MC (1984) Antimisting action of polymeric additives in jet fuels. *AIChE journal* 30(1):111–120
- Charpentier JB, Renoult MC, Crumeyrolle O, Mutabazi I (2017) Growth rate measurement in free jet experiments. *Experiments in Fluids* 58(7):89
- Christanti Y, Walker LM (2002) Effect of fluid relaxation time of dilute polymer solutions on jet breakup due to a forced disturbance. *Journal of Rheology* 46(3):733–748
- Clasen C, Phillips PM, Palangetic L, Vermant J (2012) Dispensing of rheologically complex fluids: The map of misery. *AIChE Journal* 58(10):3242–3255
- Dumouchel C (2006) A new formulation of the maximum entropy formalism to model liquid spray drop-size distribution. *Particle & Particle Systems Characterization* 23(6):468–479
- Dumouchel C (2017) Liquid atomization and spray: A multi-scale description. Keynote Lecture ASME-FEDSM, FEDSM2017-69590, V01AT04A015:1–12
- Dumouchel C, Aniszewski W, Vu TT, Ménard T (2017) Multi-scale analysis of simulated capillary instability. *International Journal of Multiphase Flow* 92:181–192
- Entov VM, Hinch EJ (1997) Effect of a spectrum of relaxation times on the capillary thinning of a filament of elastic liquid. *Journal of Non-Newtonian Fluid Mechanics* 72(1):31–53
- Entov VM, Yarin AL (1984) Influence of elastic stresses on the capillary breakup of jets of dilute polymer solutions. *Fluid Dynamics* 19(1):21–29
- Fdida N, Blaisot JB (2009) Drop size distribution measured by imaging: determination of the measurement volume by the calibration of the point spread function. *Measurement Science and Technology* 21(2):025501
- Goldin M, Yerushalmi J, Pfeffer R, Shinnar R (1969) Breakup of a laminar capillary jet of a viscoelastic fluid. *Journal of Fluid Mechanics* 38(4):689–711
- Goldin M, Pfeffer R, Shinnar R (1972) Break-up of a capillary jet of a non-newtonian fluid having a yield stress. *The Chemical Engineering Journal* 4(1):8–20
- Gordon M, Yerushalmi J, Shinnar R (1973) Instability of jets of non-newtonian fluids. *Transactions of the Society of Rheology* 17(2):303–324
- Han T, Yarin AL, Reneker DH (2008) Viscoelastic electrospun jets: Initial stresses and elongational rheometry. *Polymer* 49(6):1651–1658
- James DF, Walters K (1993) A critical appraisal of available methods for the measurement of extensional properties of mobile systems. In: *Techniques in Rheological Measurement*, Springer, pp 33–53
- Keshavarz B, Sharma V, Houze EC, Koerner MR, Moore JR, Cotts PM, Threlfall-Holmes P, McKinley GH (2015) Studying the effects of elongational properties on atomization of weakly viscoelastic solutions using rayleigh ohnesorge jetting extensional rheometry (rojer). *Journal of Non-Newtonian Fluid Mechanics* 222:171–189
- Larson RG (2005) The rheology of dilute solutions of flexible polymers: Progress and problems. *Journal of Rheology* 49(1):1–70
- Lefebvre AH, McDonell VG (2017) *Atomization and Sprays*. Taylor & Francis Group, CRC Press
- Mathues W, Formenti S, McIlroy C, Harlen OG, Clasen C (2018) Caber vs rojer—different time scales for the thinning of a weakly elastic jet. *Journal of Rheology* 62(5):1135–1153
- McKinley GH (2005) Visco-elasto-capillary thinning and break-up of complex fluids. In: DM Binding, K Walters (Eds), *Annual Rheology Reviews*, The British Society of Rheology pp 1–49
- Merrill EW, Leopairat P (1980) Scission of non-interpenetrating macromolecules in transient extensional flows. *Polymer Engineering & Science* 20(7):505–511
- Middleman S (1965) Stability of a viscoelastic jet. *Chemical Engineering Science* 20(12):1037–1040
- Mugele RA, Evans HD (1951) Droplet size distribution in sprays. *Industrial & Engineering Chemistry* 43(6):1317–1324
- Mun RP, Byars JA, Boger DV (1998) The effects of polymer concentration and molecular weight on the breakup of laminar capillary jets. *Journal of Non-Newtonian Fluid Mechanics* 74(1–3):285–297
- Nguyen TQ, Kausch HH (1988) Chain scission in transient extensional flow kinetics and molecular weight dependence. *Journal of non-newtonian fluid mechanics* 30(2–3):125–140
- Rayleigh L (1878) On the instability of jets. *Proceedings of the London mathematical society* 1(1):4–13
- Reneker DH, Yarin AL, Zussman E, Xu H (2007) Electrospinning of nanofibers from polymer solutions and melts. *Advances in applied mechanics* 41:43–346
- Rodd LE, Scott TP, Cooper-White JJ, McKinley GH (2005) Capillary break-up rheometry of low-viscosity elastic fluids. *Applied Rheology* 15(1):12–27
- Schneider CA, Rasband WS, Eliceiri KW (2012) Nih image to imagej: 25 years of image analysis. *Nature methods* 9(7):671
- Schümmer P, Tebel KH (1983) A new elongational rheometer for polymer solutions. *Journal of Non-Newtonian Fluid Mechanics* 12(3):331–347
- Sharma V, Haward SJ, Serdy J, Keshavarz B, Soderlund A, Threlfall-Holmes P, McKinley GH (2015) The rheology of aqueous solutions of ethyl hydroxy-ethyl cellulose (ehc) and its hydrophobically modified analogue (hmehec): extensional flow response in capillary break-up, jetting (rojer) and in a cross-slot extensional rheometer. *Soft Matter* 11(16):3251–3270
- Sowa WA (1992) Interpreting mean drop diameters using distribution moments. *Atomization and Sprays* 2(1):1–15
- Stelter M, Brenn G, Yarin AL, Singh RP, Durst F (2000) Validation and application of a novel elongational device for polymer solutions. *Journal of Rheology* 44(3):595–616
- Stelter M, Brenn G, Durst F (2002a) The influence of viscoelastic fluid properties on spray formation from flat-fan and pressure-swirl atomizers. *Atomization and Sprays* 12(1–3):299–327

- Stelter M, Brenn G, Yarin AL, Singh RP, Durst F (2002b) Investigation of the elongational behavior of polymer solutions by means of an elongational rheometer. *Journal of Rheology* 46(2):507–527
- Thiesset F, Dumouchel C, Ménard T, Aniszewski W, Vaudor G, Berlemont A (2019) Probing liquid atomization using probability density functions, the volume-based scale distribution and differential geometry. *Class Europe 29th european conference on Liquid Atomization and Spray Systems*
- Tirel C, Renoult MC, Dumouchel C, Lisiecki D, Crumeyrolle O, Mutabazi I (2017) Multi-scale analysis of a viscoelastic liquid jet. *Journal of Non-Newtonian Fluid Mechanics* 245:1–10
- Tirtaatmadja V, McKinley GH, Cooper-White JJ (2006) Drop formation and breakup of low viscosity elastic fluids: Effects of molecular weight and concentration. *Physics of fluids* 18(4):043101–043118
- Yarin AL (1991) Strong flows of polymeric liquids part 2. mechanical degradation of macromolecules. *Journal of non-newtonian fluid mechanics* 38(2-3):127–136
- Yarin AL (1993) *Free liquid jets and films: hydrodynamics and rheology*. Longman Scientific & Technical and Wiley & Sons, Harlow, New York
- Yon J (2003) *Jet diesel haute pression en champ proche et lointain: Etude par imagerie*. PhD thesis, Université de Rouen